

ANALYSIS OF THE CUP-CONE FRACTURE IN A ROUND TENSILE BAR

V. TVERGAARD

Department of Solid Mechanics, The Technical University of Denmark, Lyngby, Denmark

and

A. NEEDLEMAN

Division of Engineering, Brown University Providence, RI 02912, U.S.A.

(Received 4 May 1983)

Abstract—Necking and failure in a round tensile test specimen is analysed numerically, based on a set of elastic–plastic constitutive relations that account for the nucleation and growth of micro-voids. Final material failure by coalescence of voids, at a value of the void volume fraction in accord with experimental and computational results, is incorporated in this constitutive model via the dependence of the yield condition on the void volume fraction. In the analyses the material has no voids initially; but high voidage develops in the centre of the neck where the hydrostatic tension peaks, leading to the formation of a macroscopic crack as the material stress carrying capacity vanishes. The numerically computed crack is approximately plane in the central part of the neck, but closer to the free surface the crack propagates on a zig-zag path, finally forming the cone of the cup-cone fracture. The onset of macroscopic fracture is found to be associated with a sharp “knee” on the load deformation curve, as is also observed experimentally, and at this point the reduction in cross-sectional area stops.

Résumé—Nous avons analysé numériquement la striction et la rupture d'un échantillon de traction cylindrique, à partir d'un ensemble de relations constitutives élastico-plastiques qui rendent compte de la germination et de la croissance des micro-cavités. Nous introduisons dans ce modèle constitutif la rupture finale du matériau par coalescence des cavités, pour une fraction volumique des cavités en accord avec les résultats expérimentaux et théoriques, par l'intermédiaire de la variation de la limite élastique en fonction de la fraction volumique des cavités. Dans nos analyses, le matériau ne présente initialement pas de cavités; mais une forte cavitation se produit au centre de la striction où la tension hydrostatique passe par un maximum, conduisant à la formation d'une fissure macroscopique lorsque la capacité du matériau à supporter une contrainte tend vers zéro. La fissure calculée numériquement est approximativement plane dans la partie centrale de la striction, mais au voisinage de la surface libre la fissure se propage en zig-zag, formant finalement le cône de la rupture en cône et cuvette. Le début de la rupture macroscopique est associé à un conde aigu sur la courbe charge-déformation, que l'on observe également expérimentalement; à ce moment là, la diminution de la surface de la section de l'éprouvette s'arrête.

Zusammenfassung—Das Einschnür- und Bruchverhalten von runden Zugproben wird numerisch analysiert. Die Rechnungen gehen aus von einem Satz elastisch-plastischer Grundgleichungen, die die Keimbildung und das Wachsen von Mikrohohlräumen berücksichtigen. Der Bruch durch das Zusammenwachsen der Hohlräume wobei experimenteller und theoretischer Wert des Volumanteiles der Hohlräume übereinstimmen wird dadurch in dieses Modell eingeführt, daß die Fließbedingung von dem Volumanteil der Hohlräume abhängt. Bei der Analyse besitzt das Material anfangs keine Hohlräume. Im Zentrum der Einschnürung jedoch, wo die hydrostatische Zugkomponente ein Maximum aufweist, bilden sich viele Hohlräume. Das führt zu einem makroskopischen Riß, wenn das Material die anglegte Spannung nicht mehr tragen kann. Der numerisch berechnete Riß ist im Zentrum der Einschnürung nahezu eben. Näher an der Oberfläche jedoch verläuft er zickzack-förmig und bildet schließlich den Kegel der Bruchfläche. Der makroskopische Bruch hängt, wie auch experimentell beobachtet wird, mit dem Auftreten eines scharfen “Knies” in der Verformungskurve zusammen. Bei diesem Knie ist die Verringerung der Querschnittsfläche beendet.

1. INTRODUCTION

The round bar tensile test is widely used for investigating the effects of mechanical properties on ductility. Figure 1, taken from Bluhm and Morrissey [1], illustrates a representative sequence of events. Void formation was first detected, by an ultrasonic technique, at the point marked “incipient fracture”, and insert “H” depicts the state of the neck somewhat beyond this point. Bluhm and Morrissey [1] attribute

the subsequent sharp “knee” in the load–deflection curve to the beginning of gross shear deformation with an associated coalescence of voids leading to a central crack (insert “M”). The crack grows in a zig-zag fashion, remaining near the plane of minimum cross-section, until it undergoes one final large zig (or zag) to the surface to form the cone of the cup-cone fracture.

A variety of experimental and analytical investigations have lead to a basic understanding of the

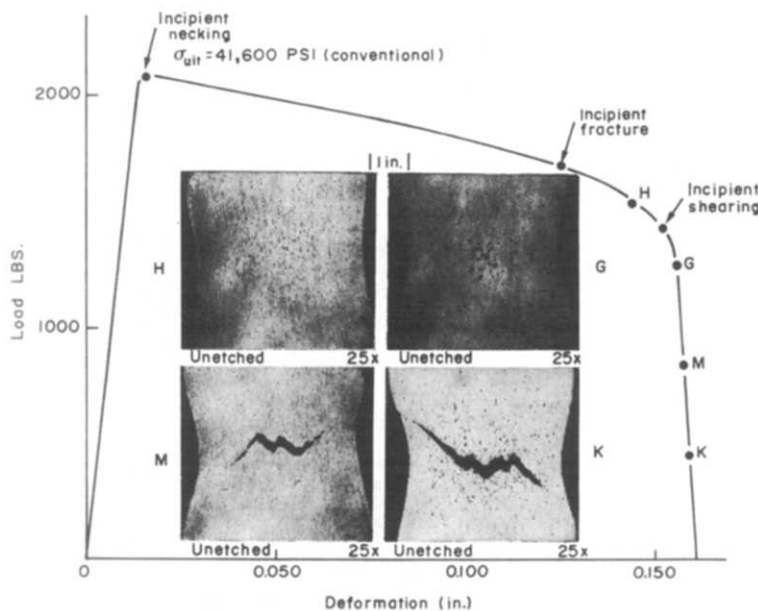


Fig. 1. Failure process in the neck of a round tensile specimen of copper, correlated with the load deformation curve (from Bluhm and Morrissey [1]).

micro-mechanics of the fracture process depicted in Fig. 1, although a quantitative theory of ductile rupture remains to be developed. Puttick [2] showed that cavities in polycrystalline copper deformed at room temperature, as in Fig. 1, originate from inclusions. Subsequent observations, reviewed by Goods and Brown [3], demonstrated the central role played by inclusion cracking and/or debonding in nucleating voids in structural metals, which then grow by plastic deformation of the surrounding matrix material. Analyses of an isolated void in a plastically deforming solid (McClintock [4]; Rice and Tracey [5]) have been used to estimate the onset of coalescence by necking down of the ligament between the voids. Such analyses can overestimate, by a wide margin, the strain at which coalescence occurs. This overestimate arises because internal necking between cavities is interrupted by localized shear, Cox and Low [6], Rogers [7], Green and Knott [8] and Hancock and Mackenzie [9]. Observations, e.g. Hancock and Mackenzie [9], and approximate models, Brown and Embury [10], indicate that coalescence by localized shear takes place when the void spacing is a constant of order unity times the void length.

Aspects of these features of a progressively cavitating solid have been incorporated into a phenomenological constitutive framework by Gurson [11,12]. Based on an approximate analysis of a rigid-plastic solid with a spherical cavity, Gurson [11,12] developed a plastic flow rule for a void containing ductile solid. This constitutive relation has been employed in a number of studies of aspects of the ductile rupture process, e.g. [13-17]. Some of these investigations have led to proposed

modifications of the original Gurson model, Tvergaard [14, 16], to obtain improved agreement with the predictions of more detailed models of void growth and to explicitly account for void coalescence at the representative void spacings noted above.

Here we carry out a finite element analysis of necking and failure in the tensile test employing Gurson's constitutive relation [11, 12]. Previous numerical solutions for the tensile test, e.g. Needleman [18], Norris *et al.* [19] and Saje [20], as well as the classical Bridgman [21] solution, have played a useful role in assessing the conditions governing fracture initiation, Argon *et al.* [22-24], Hancock and Mackenzie [9] and Hancock and Brown [25]. However, once micro-rupture initiates, the assumptions underlying these analyses are no longer appropriate. Very little is known about the conditions prevailing in the specimen during progressive failure.

Our present calculations follow the inception of necking, through the initiation and growth of voids in the center of the neck, to the linking up of these voids in a central crack, which propagates across the specimen. The numerical results reproduce the essential features of tensile fracture exhibited in Fig. 1. For example, the central crack, once initiated, zig-zags in a characteristic fashion as it propagates across the specimen to the free surface, ultimately forming the familiar cup-cone fracture.

2. A MODEL FOR VOID NUCLEATION, GROWTH AND COALESCENCE

An elastic-plastic material model that accounts for the nucleation and growth of microscopic voids in a

ductile metal has been developed by Gurson [11, 12]. This model refers to an approximate yield condition, of the form $\Phi(\sigma^y, \sigma_M, f) = 0$, for a porous ductile material, where σ^y is the average macroscopic Cauchy stress tensor, σ_M is an equivalent tensile flow stress representing the actual microscopic stress-state in the matrix material, and f is the current void volume fraction.

The complete loss of material stress-carrying capacity at ductile fracture, due to the coalescence of voids, is not predicted at a realistic level of the void volume fraction by Gurson's equations. Experimental studies discussed by Brown and Embury [10] and Goods and Brown [3] indicate that coalescence of two neighbouring voids occurs approximately when their length has grown to the order of magnitude of their spacing. This local failure occurs by the development of slip planes between the cavities or simply necking of the ligament. An estimate of the critical void volume fraction, obtained in [10] by a simple model, is f_c of the order of 0.15.

Based on these experimental coalescence results it seems reasonable to limit the direct application of the Gurson model to void volume fractions below a certain critical value f_c , and to modify the equations above f_c . Such models of final material failure have been discussed by Tvergaard [16], who introduced an extra contribution, $(f')_{\text{failure}}$, to be added to the usual expression

$$\dot{f} = (\dot{f})_{\text{growth}} + (\dot{f})_{\text{nucleation}} \quad (2.1)$$

for the change of void volume fraction during an increment of deformation. Here $(\dot{})$ denotes a small increment. In the present investigation an alternative failure model shall be employed, in which the approximate yield condition $\Phi = 0$ is modified for $f > f_c$.

All equations in the following will be given in the context of a Lagrangian formulation of the field equations. A material point is identified by the coordinates x^i in the reference configuration, and the metric tensors in the current configuration and the reference configuration are denoted by G_y and g_y , respectively, with determinants G and g . The Lagrangian strain tensor is $\eta_y = 1/2(G_y - g_y)$, and the contravariant components of the Kirchhoff stress tensor τ^y on the embedded deformed coordinates, to be used subsequently, are related to average macroscopic Cauchy stresses by $\tau^y = \sqrt{G/g} \sigma^y$. Indices range from 1 to 3, and the summation convention is adopted for repeated indices.

The approximate yield condition to be used here is of the form

$$\Phi = \frac{\sigma_e^2}{\sigma_M^2} + 2f^* q_1 \cosh \left\{ \frac{\sigma_k^k}{2\sigma_M} \right\} - \{1 + (q_1 f^*)^2\} = 0 \quad (2.2)$$

where the macroscopic Mises stress is $\sigma_e = (3s_y s_y / 2)^{1/2}$, in terms of the stress deviator $s_y = \sigma_y - G^y \sigma_k^k / 3$, and $\sigma_k^k / 3$ is the macroscopic mean

stress. For $f^* = f$ and $q_1 = 1$ the expression (2.2) is that derived by Gurson [11] based on a rigid-perfectly plastic upper bound solution for spherically symmetric deformations around a single spherical void. The additional parameter q_1 was introduced by Tvergaard [14, 26], who found that the agreement with numerical studies of materials containing periodically distributed circular cylindrical or spherical voids is considerably improved by using $q_1 = 1.5$ in (2.2). Thus, the value $q_1 = 1.5$ is applied here to improve the predictions at small void volume fractions; but has nothing to do with the model of final failure.

The modification of the yield condition, to account for final material failure, is introduced through the function $f^*(f)$ specified by

$$f^* = \begin{cases} f & , \text{ for } f \leq f_c \\ f_c + K(f - f_c) & , \text{ for } f > f_c. \end{cases} \quad (2.3)$$

It is noted that the ultimate value, $f^* = f_U^*$, at which the macroscopic stress carrying capacity vanishes, is given by $f_U^* = 1/q_1$ according to (2.2). Plots of the yield function in Fig. 2 illustrate how the material loses its stress carrying capacity for $f^*/f_U^* \rightarrow 1$. Now, if experiments or analyses indicate that the void volume fraction at final fracture is $f = f_F$, the value of the constant K to be used in (2.3) is directly given by the requirement $f^*(f_F) = f_U^*$

$$K = \frac{f_U^* - f_c}{f_F - f_c}. \quad (2.4)$$

If the yield function was not modified, the void volume fraction at fracture f_F would appear as f_U^* ; but this would represent an unrealistically large value of f_F , both for $q_1 = 1$ and for $q_1 = 1.5$.

The experiments discussed by Brown and Embury [10] and Goods and Brown [3] indicate coalescence at values of f around 0.15; certainly not much larger than 0.2. Furthermore, numerical model analyses by Andersson [27] show $f \approx 0.25$ at fracture, obtained by considering initially spherical voids in a rigid-perfectly plastic matrix, with only one of the principal macroscopic strains different from zero (a highly triaxial stress state). Based on these experimental and computational results the values $f_c = 0.15$ and $f_F = 0.25$ are employed in the present investigation.

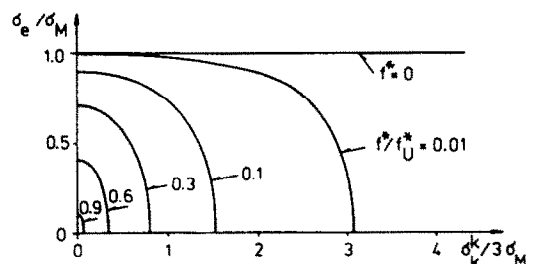


Fig. 2. Yield surface dependence on the hydrostatic tension for various values of the function f^* in equation (2.2).

The failure model introduced here is very similar to that used previously [16, 28]. For $f \leq f_c$ the descriptions are identical, and for $f > f_c$ the material stress carrying capacity is more rapidly reduced to zero than predicted by the Gurson model. However, introducing the modified yield function, as specified by (2.2) and (2.3), may be more attractive from a physical point of view than the addition of an extra failure term to (2.1).

In the Gurson model the effective plastic strain ϵ_M^p , representing the microscopic strain-state in the matrix material, is assumed to be related to σ_M through a uniaxial true stress natural strain curve, and to satisfy an equivalent plastic work expression

$$\dot{\epsilon}_M^p = \left(\frac{1}{E_i} - \frac{1}{E} \right) \dot{\sigma}_M, \quad \sigma^u \dot{\eta}_{ij}^p = (1-f) \sigma_M \dot{\epsilon}_M^p. \quad (2.5)$$

Here, E is Young's modulus, E_i is the current tangent modulus, and $\dot{\eta}_{ij}^p$ is the plastic part of the macroscopic strain increment. An expression for $\dot{\sigma}_M$ is obtained from these two equations by eliminating $\dot{\epsilon}_M^p$.

The change of the void volume fraction (2.1) during an increment of deformation results partly from the growth of existing voids

$$(\dot{f})_{\text{growth}} = (1-f) G^u \dot{\eta}_{ij}^p \quad (2.6)$$

and partly from the nucleation of new voids. Various nucleation criteria have been formulated within this general phenomenological framework (Gurson [11, 12]; Needleman and Rice [29]). Here we employ a plastic strain controlled nucleation criterion suggested by Gurson's [11, 12] analysis of data obtained by Gurland [30]. The increase in the void volume fraction due to the nucleation of new voids is given by

$$(\dot{f})_{\text{nucleation}} = A \dot{\sigma}_M \quad (2.7)$$

where $\dot{\sigma}_M$ ($\dot{\epsilon}_M^p$) is specified by (2.5) and the parameter A is chosen so that nucleation follows a normal distribution as suggested by Chu and Needleman [13]. Then, with a volume fraction f_N of void nucleating particles, a mean strain for nucleation ϵ_N and a standard deviation s_N

$$A = \left(\frac{1}{E_i} - \frac{1}{E} \right) \frac{f_N}{s_N \sqrt{2\pi}} \exp \left[-\frac{1}{2} \left(\frac{\epsilon_M^p - \epsilon_N}{s_N} \right)^2 \right] \quad (2.8)$$

This nonzero value of A is only used if ϵ_M^p exceeds its current maximum in the increment considered; otherwise $A = 0$.

The plastic part of the macroscopic strain rate is taken to be proportional with the normal $\partial\Phi/\partial\sigma^u$ of the yield function, since normality for the matrix material implies macroscopic normality (Berg [31]). Then, using the consistency condition $\dot{\Phi} = 0$ together with equations (2.1) and (2.5)–(2.7) we find

$$\dot{\eta}_{ij}^p = \frac{1}{H} m_{ij} m_{kl} \dot{\sigma}^{kl} \quad (2.9)$$

where $\dot{\sigma}^{kl}$ is the Jaumann (co-rotational) rate of the

Cauchy stress tensor and

$$m_{ij} = \frac{3}{2} \frac{s_{ij}}{\sigma_M} + \alpha G_{ij}, \quad \alpha = \frac{f^*}{2} q_1 \sinh \left(\frac{\sigma_k^k}{2\sigma_M} \right) \quad (2.10)$$

$$H = \frac{\sigma_M}{2} \left[-3\alpha(1-f) \frac{\partial\Phi}{\partial f} - \left(\frac{\partial\Phi}{\partial f} A + \frac{\partial\Phi}{\partial\sigma_M} \right) \times \frac{EE_i}{E-E_i} \frac{1}{1-f} \left(\frac{\sigma_e^2}{\sigma_M^2} + \alpha \frac{\sigma_k^k}{\sigma_M} \right) \right] \quad (2.11)$$

Plastic yielding initiates when $\Phi = 0$ for $\Phi > 0$, and continued plastic yielding requires $\Phi = 0$ and

$$\frac{1}{H} m_{kl} \dot{\sigma}^{kl} \geq 0.$$

It is noted that the modification of Φ by the function f^* enters the expressions through α and $\partial\Phi/\partial f$.

The total strain rate is taken to be the sum of the elastic and plastic parts, $\dot{\eta}^u = \dot{\eta}_{ij}^e + \dot{\eta}_{ij}^p$, where

$$\dot{\eta}_{ij}^e = \frac{1}{E} \{ (1+\nu) G_{ik} G_{jl} - \nu G_{ij} G_{kl} \} \dot{\sigma}^{kl} \quad (2.12)$$

and ν is Poisson's ratio. The inverse of this sum is of the form $\dot{\sigma}^u = R^{ijkl} \dot{\eta}_{kl}$, which can be transformed into the incremental constitutive relations

$$\dot{\tau}^u = L^{ijkl} \dot{\eta}_{kl}. \quad (2.13)$$

Detailed expressions for the instantaneous moduli L^{ijkl} , which are in general non-symmetric ($L^{ijkl} \neq L^{klij}$), are given in [14, 15, 28] and shall not be repeated here.

The uniaxial true stress-logarithmic strain curve for the matrix material is represented by the piecewise power law

$$\epsilon = \begin{cases} \frac{\sigma}{E}, & \text{for } \sigma \leq \sigma_y, \\ \frac{\sigma_y}{E} \left(\frac{\sigma}{\sigma_y} \right)^n, & \text{for } \sigma > \sigma_y, \end{cases} \quad (2.14)$$

where σ_y is the uniaxial yield stress, and n is the strain hardening exponent.

We conclude this section by illustrating the effect of the constitutive relation on a homogeneously deformed material element. Two deformation histories are considered. One is uniaxial axisymmetric tension, and the other is axisymmetric tension with a superposed hydrostatic tension. The hydrostatic tension history is taken to be that experienced by a material element at the center of a neck. As described by Saje *et al.* [15], Bridgman's [21] solution for the stress state at the minimum section is employed to model this enhanced triaxiality. The material parameters are taken as those used in the numerical calculations described subsequently. The elastic-plastic properties of the matrix material are specified by $\sigma_y/E = 0.0033$, $\nu = 0.3$ and $n = 10$, and $q_1 = 1.5$ is used. The plastic strain controlled nucleation is described by the volume fraction $f_N = 0.04$ of void nucleating particles, the mean strain for nucleation

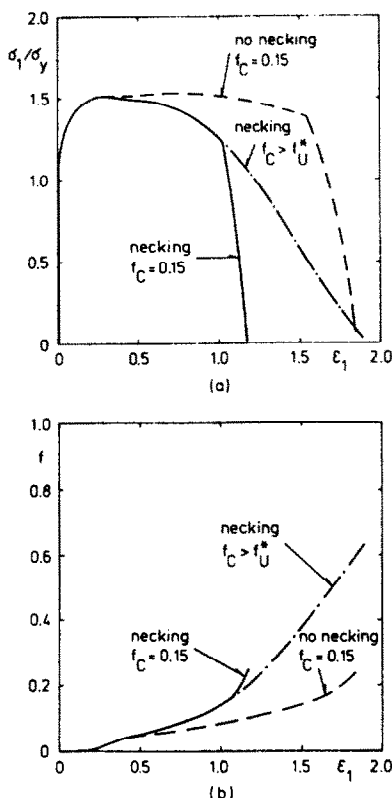


Fig. 3. Effect of the model for void nucleation, growth and coalescence in axisymmetric tension. Necking refers to Bridgman's solution. (a) True macroscopic tensile stress vs logarithmic strain. (b) Void volume fraction vs logarithmic strain.

$\epsilon_N = 0.3$, and the standard deviation $s_N = 0.1$ in (2.8), and the initial void volume fraction is zero.

Figure 3(a) displays the true macroscopic tensile stress σ_1 in the aggregate, normalized by the matrix yield strength, as a function of the imposed logarithmic tensile strain ϵ_1 . For the curve marked $f_c > f^*$, the function f^* is identically equal to the void volume fraction f throughout the deformation history. Necking is taken to initiate when the Considere criterion is satisfied, i.e. at $\epsilon_1 = 0.1$. The burst of nucleation around $\epsilon_1 = 0.3$ leads to a drop in true stress for the aggregate [the matrix is still strain hardening via (2.14)]. For the curves marked $f_c = 0.15$, we also use $f_f = 0.25$ in (2.4).

Figure 3(b) shows the void volume fraction as a function of tensile strain. The hydrostatic tension associated with "necking" leads to substantially enhanced void growth and this in turn induces the relatively rapid drop in stress carrying capacity for the cases with necking in Fig. 3(a). When $f^* \equiv f$, complete loss of stress carrying capacity occurs at $f = 2/3$, which for the tensile deformation history with "necking" occurs at a logarithmic tensile strain of 1.9. For the two other curves in Fig. 3(a) the stress carrying capacity drops rapidly once $f = f_c$. When the imposed deformation state is purely axisymmetric

tension, with no superposed triaxiality, the true tensile stress falls slowly until $f = f_c$ then the stress drops abruptly, with the complete loss of stress carrying capacity occurring at $\epsilon_1 = 1.84$. The superposed hydrostatic tension results in this complete loss of stress carrying capacity at a substantially smaller strain, $\epsilon_1 = 1.17$.

3. METHOD OF ANALYSIS

A cylindrical reference coordinate system is used for the analysis of the round tensile bar, with axial coordinate x^1 , radial coordinate x^2 , and circumferential angle x^3 . Attention is confined to *axisymmetric* deformations so that all field quantities are independent of x^3 .

In terms of the displacement components u^i on the reference base vectors the Lagrangian strain tensor is given by

$$\eta_{ij} = \frac{1}{2} (u_{i,j} + u_{j,i} + u_{,j}^k u_{k,i}) \quad (3.1)$$

where $(\)_{,j}$ denotes covariant differentiation in the reference frame. The requirement of equilibrium is specified in terms of the principle of virtual work

$$\int_V \tau^{ij} \delta \eta_{ij} dV = \int_S T^i \delta u_i dS. \quad (3.2)$$

Here, V and S are the volume and surface, respectively, of the body in the reference configuration, and $T^i = (\tau^{ij} + \tau^{kj} u_{,k}^i) n_j$ are the specified nominal tractions on a surface with reference normal n_j .

The initial length and the initial radius of the tensile specimen to be analysed are $2L_0$ and R_0 , respectively, and symmetry about the mid-plane, $x^1 = 0$, is assumed, so that only half of the bar needs to be analysed, as indicated in Fig. 4. In the numerical analyses a small initial thickness inhomogeneity ΔR is assumed of the form

$$\Delta R = -\zeta R_0 \cos \frac{\pi x^1}{L_0} \quad (3.3)$$

to ensure that necking takes place at the centre of the bar. The boundary conditions for the axisymmetric body to be analysed are specified as

$$T^1 = 0 \quad \text{for} \quad x^2 = R_0 + \Delta R \quad (3.4)$$

$$u^1 = 0 \quad \text{and} \quad T^2 = 0 \quad \text{for} \quad x^1 = 0 \quad (3.5)$$

$$u^1 = U \quad \text{and} \quad T^2 = 0 \quad \text{for} \quad x^1 = L_0. \quad (3.6)$$

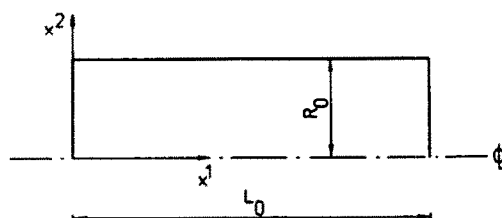


Fig. 4. Region analysed numerically for round tensile bar.

Here, U is a uniform end displacement, such that $\epsilon_a = \ln(1 + U/L_0)$ is the average logarithmic strain.

Numerical solutions are obtained by a linear incremental method, making use of the incremental constitutive relations (2.13). The current values of all field quantities, e.g. stresses τ^y , strains η_y , void volume fraction f , are assumed known, and an increment \dot{U} of the end displacement is prescribed. Expanding the principle of virtual work (3.2) about this known state gives to lowest order

$$\int_V \{ \tau^y \delta \eta_y + \tau^y \dot{u}_i^y \delta u_{i,j} \} dV = \int_S \dot{T}^i \delta u_i dS - \left[\int_V \tau^y \delta \eta_y dV - \int_S T^i \delta u_i dS \right]. \quad (3.7)$$

The terms bracketed in this equation vanish, if the given state is precisely an equilibrium state, but are included here to prevent drifting of the solution away from the true equilibrium path.

In the incremental finite element solution the mesh used over the region shown in Fig. 4 consists of quadrilaterals, each built up of four triangular, axisymmetric, linear displacement elements. The integrals in (3.7) are evaluated at one central point within each element. As in previous plane strain analyses [17, 28] the active branch of the tensor of moduli $L^{\mu\kappa}$ to be used in an integration point is chosen on the basis of the previous increment, such that the plastic branch is used if the conditions for plastic loading were satisfied in that increment. This procedure has been found sufficiently accurate, as long as small increments are used.

During the final failure process the end displacement U may grow very little or even decay, while the load drops rapidly. In such cases numerical problems in the solution of (3.7) are avoided by using a mixed Rayleigh-Ritz-finite element method [32] to prescribe negative load increments rather than the end displacement.

The primary focus here is on the formation and subsequent growth of a crack inside the neck of a tensile specimen. Therefore, the application of a material description that accounts for the growth of microscopic voids and attempts to model the final material failure by void coalescence is essential here. The set of constitutive relations presented in Section 2 provide such a material model, and this model contains a fracture criterion, since the material stress carrying capacity disappears for $f \rightarrow f_F$ (or for $f^* \rightarrow f_F^*$). In each particular material point the prediction of fracture depends on the stress and strain path that has been followed, and of course on the parameter values used to describe nucleation models, final material failure, and matrix material plasticity.

Numerically, the crack formation is introduced by an element-vanish-technique, which has also been applied by Tvergaard [28] under plane strain conditions. When failure occurs in an element, this element is taken to vanish; but the computation is continued

with the empty element, without changing the nodal points. In order to avoid poor numerical stability associated with nearly failed elements, the elements are in fact taken to vanish slightly before final failure, at $f^* = 0.9 f_F^*$, and the nodal forces arising from the small remaining stresses in the nearly failed element are stepped down to zero over a few subsequent increments.

In a homogeneous cylindrical bar necking initiates at a bifurcation point, as has been studied in detail by Hutchinson and Miles [33], for an incompressible elastic-plastic material. For a long thin bar this bifurcation takes place at the load maximum, whereas for more stubby specimens bifurcation is somewhat delayed. In the present paper the location of this instability point shall not be further analysed, even though the porous ductile material, with a significant plastic dilatancy, is not covered by the analysis of [33]. A more detailed study could be based on upper and lower bound analyses suggested by Raniecki and Bruhns [34], as has been done under plane strain conditions [28]. For the bars with the small imperfection (3.3), to be discussed in the following section, the necking delay is determined by the numerical analyses.

The possibility of plastic flow localization into a shear band is of considerable interest in a study of ductile fracture. Such localization in porous ductile metals has been analysed by a number of authors [15, 16, 35], based on a simple model (see Fig. 5). An initial material inhomogeneity is assumed inside a thin, plane slice of material and the stress state inside and outside this slice, respectively, is assumed to remain homogeneous throughout the deformation history. The principal directions outside the band are assumed to remain fixed, parallel with Cartesian reference coordinates x^i , with the major principal stress in the x^1 -direction. Furthermore, the band has the initial angle of inclination ψ , and the unit normal n_i , and is parallel with the x^3 -axis. Then, the requirement of compatibility over the band interface is specified by

$$u_{a,\beta}^b = u_{a,\beta}^o + c_a n_\beta, \quad u_{3,3}^b = u_{3,3}^o \quad (3.8)$$

and the corresponding equilibrium condition is

$$(T^\alpha)^b = (T^\alpha)^o \quad (3.9)$$

where $()^b$ and $()^o$ denote quantities inside and outside the band, respectively, and Greek indices range from 1 to 2. These two equations, with only two variables c_1 and c_2 , govern shear band development in a homogeneously stretched material.

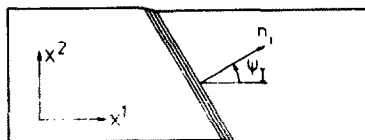


Fig. 5. Shear band in a homogeneously strained solid.

If there is no initial inhomogeneity, the first bifurcation into a shear band mode predicted by (3.8) and (3.9), for any band inclination, coincides with the loss of ellipticity of the equations governing incremental equilibrium. Such predictions for the porous ductile material model have been used by Yamamoto [35] and by Needleman and Rice [29] to discuss the much higher ductility under uniaxial, axisymmetric tension than that under plane strain tension. The exceedingly large localization strains in uniaxial axisymmetric tension (ϵ_1 far above unity) are somewhat reduced by assuming a realistic inhomogeneity of the initial void volume fraction, and even further reduced by accounting for the development of a triaxial axisymmetric stress state due to necking; but still on this basis Saje *et al.* [15] find localization strains of the order of unity. The most critical final angle of inclination ψ of localized shear bands found in these investigations is around 40° to 45° .

In the numerical solutions, to be considered in the present paper, the formation of a skew shear band across the whole bar, as that indicated in Fig. 5, is excluded by the assumption of axisymmetric solutions. However, in the highly strained neck region, where the deformations are nonuniform, loss of ellipticity will also occur axisymmetrically and the characteristic surface defining the critical direction for shear bands will tend to be conical.

4. NUMERICAL FAILURE RESULTS

The material to be analysed is that also considered in Fig. 3, with the volume fraction $f_N = 0.04$ of void nucleating particles, the mean strain for nucleation $\epsilon_N = 0.3$, and the corresponding standard deviation $s_N = 0.1$, in (2.8). The initial void volume fraction is assumed to be zero, $f_i = 0$, and the parameter $q_1 = 1.5$ is used in the yield condition (2.2), as suggested in [14, 26]. Furthermore, the elastic-plastic properties of the matrix material are specified by the parameters $\sigma_y/E = 0.0033$, $\nu = 0.3$ and $n = 10$, and final material failure is taken to be characterized by the parameters $f_c = 0.15$ and $f_f = 0.25$ in (2.3) and (2.4), as discussed in Section 2.

The behaviour of this particular material under uniaxial plane strain tension has been analysed in detail by Tvergaard [28]. In those circumstances loss of ellipticity occurs at the logarithmic strain $\epsilon_1 = 0.23$. Numerical computations in [28] show the formation of shear bands and the subsequent growth of the localized deformations, until final fracture occurs by void coalescence inside the bands, in a so-called void sheet. These numerical results were very dependent on designing the mesh such that shear bands form along the quadrilateral element diagonals, at the critical strain.

In the case of the round tensile bars the critical strain for shear band formation is unrealistically high. Therefore, the appropriate mesh design is expected to be controlled by more complex mechanisms

here, than those found under plane strain tension [28, 36]. To investigate this, initial computations have been carried out with a uniform mesh in the neck region, and a continuously growing mesh-size outside this region. Three different initial aspect ratios of the quadrilaterals in the neck region have been tried, with 8 quadrilaterals in the x^2 -direction and 32 quadrilaterals in the x^1 -direction. The initial imperfection (3.3) is specified by $\xi = 0.001$, and the initial length to radius ratio is given by $L_0/R_0 = 4$.

The behaviour found in all three cases, after necking, is characterized by the development of hydrostatic tension in the neck and a corresponding rapid void growth until fracture occurs at the centre ($x^1 = x^2 = 0$), long before the critical strain for shear bands is reached. Subsequently, a penny-shaped crack grows in the plane $x^1 = 0$. Each of these three computations with relatively crude meshes predict final separation by a plane fracture surface.

To refine the mesh in the region of interest a continuously growing mesh-size is also introduced in the radial direction, in the central part of the bar. A result obtained by such a doubly stretched 8×32 mesh is shown in Fig. 6. At the stage illustrated, the penny-shaped crack has grown approximately half-way from the centre to the external surface, and the figure shows the deformed mesh, curves of constant void volume fraction f , and curves of constant maximum principal logarithmic strain ϵ , respectively. The average logarithmic strain in Fig. 6 is $\epsilon_a = 0.177$ and the load T , normalized by its maximum value T_{\max} , is $T/T_{\max} = 0.418$. The strain contours in Fig. 6(c) do indicate a tendency towards localization at an inclination away from the x^2 -axis; but even though this indication is much clearer here than found in the three initial computations, the crack continues to grow along the mid-plane until final separation.

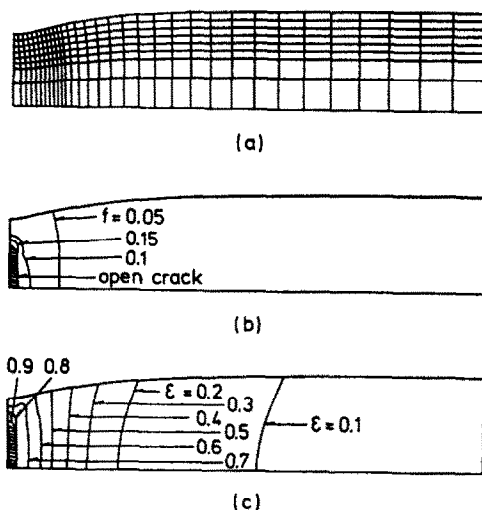


Fig. 6. Solution at $T/T_{\max} = 0.418$ and $\epsilon_a = 0.177$, for $L_0/R_0 = 4$. (a) Deformed mesh 8×32 mesh. (b) Curves of constant void volume fraction. (c) Curves of constant maximum principal logarithmic strain.

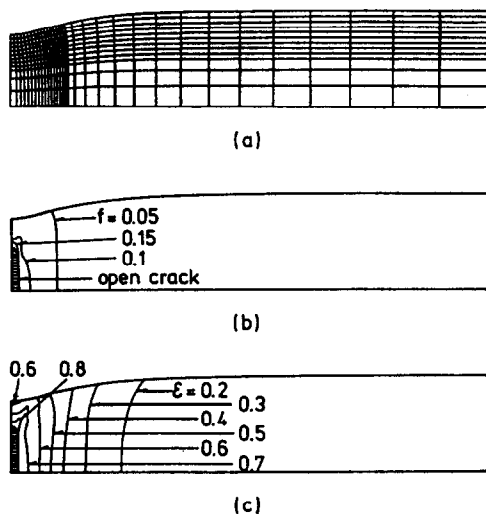


Fig. 7. Solution at $T/T_{\max} = 0.372$ and $\epsilon_e = 0.189$, for $L_0/R_0 = 4$. (a) Deformed 12×32 mesh. (b) Curves of constant void volume fraction. (c) Curves of constant maximum principal logarithmic strain.

The mesh designs are chosen such that the diagonals are inclined approximately 40° relative to the x^2 -axis, when the process reaches a stage as that shown in Fig. 6. The three initial computations, indicated most strain intensification away from the x^2 -axis for diagonals inclined about 40° , and this also agrees with the critical angles of shear band inclination found by Saje *et al.* [15]. Furthermore, the strain state near the tip of a penny-shaped crack in a plastic material is characterized by a very high level of strain at about 45° relative to the crack plane (see He and Hutchinson [37]).

It should be noticed now that the initial mesh design required for an analysis of final failure in a round tensile bar is essentially controlled by the first occurrence of fracture at the centre of the neck. When the crack initiates, elastic unloading takes place at $x^2 = 0$ on the crack surface, and all material near the x^1 -axis remains elastically unloaded throughout the remaining fracture process. In fact, as the penny-shaped crack grows, plasticity is limited to an axisymmetric, triangular region in front of the crack tip. This means that the angle of inclination of the mesh diagonals changes very little after the first occurrence of fracture. Furthermore, the average strain ϵ_e will remain nearly constant after crack initiation, as only the opening of the crack and elastic changes of the strain along the x^1 -axis will contribute to ϵ_e . We note the significant difference from the behaviour found for the plane strain tensile test [28, 36], where flow localization terminates the smooth deformation field in the neck, and failure occurs subsequently by crack propagation inside a localized shear band.

Since the critical strain for shear bands is not reached prior to fracture in the round bar, the possibility of out-of-plane crack growth must rely on

the strain concentrations at the crack tip. The near tip fields are very poorly represented by the crude meshes used in the initial computations, and therefore further refinements are tried. Figure 7 shows results obtained by a 12×32 mesh, at a stage identified by $T/T_{\max} = 0.372$ and $\epsilon_e = 0.189$. Here, the inclined strain intensification is more pronounced than that of Fig. 6, and even the void volume fraction contours show a slight out-of-plane tendency; but finally the mode of in-plane crack growth dominates, also in this case. It should be emphasized that the stages of the fracture processes illustrated in Figs 6 and 7, where the penny-shaped cracks have grown a little beyond half the external neck radius, are those at which most of the inclined strain intensification has been found. The general strain patterns inside the neck, shown in Figs 6(c) and 7(c), are in good agreement; but too late necking was predicted in the case of Fig. 7, as a result of the highly distorted initial mesh.

Crack growth out of the plane of the initial penny-shaped crack is predicted in the next computation, for a much finer mesh, and therefore this computation will be discussed in more detail. A rather stubby specimen, $L_0/R_0 = 2$, is considered here, since we are only interested in the neck region, and the initial 20×42 mesh is shown in Fig. 8. This mesh is still crude in relation to crack tip fields, but fine enough to show the cup-cone fracture mechanism.

The calculated load vs average axial strain curve is shown by the solid curve in Fig. 9. Necking occurs where the curve deviates from that corresponding to continued homogeneous straining, which takes place considerably after the load maximum, due to the small value of L_0/R_0 . For comparison, Fig. 9 also includes the load vs average axial strain curve corresponding to the same tensile test specimen with no voids, $f \equiv 0$. It is seen that necking occurs at approximately the same strain for the solid and dotted curves, respectively, but subsequently the load decays more rapidly for the specimen in which voids nucleate and grow. Fracture initiates at $T/T_{\max} = 0.727$, and subsequently the average strain ϵ_e cannot change much, as discussed above.

Figures 10, 11 and 12 show deformed meshes, curves of constant void volume fraction f , and curves of constant maximum principal logarithmic strain ϵ , respectively, at five different stages of the fracture process. The load levels T/T_{\max} at these five stages are 0.731, 0.521, 0.431, 0.153 and 0.032, respectively, and the strains ϵ_e are 0.267, 0.270, 0.272, 0.277 and 0.278.

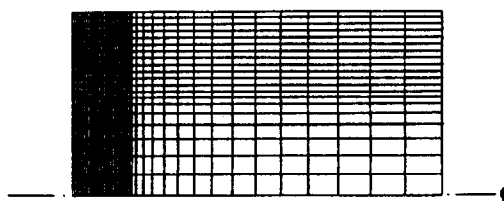


Fig. 8. Initial 20×42 mesh for a stubby specimen $L_0/R_0 = 2$.

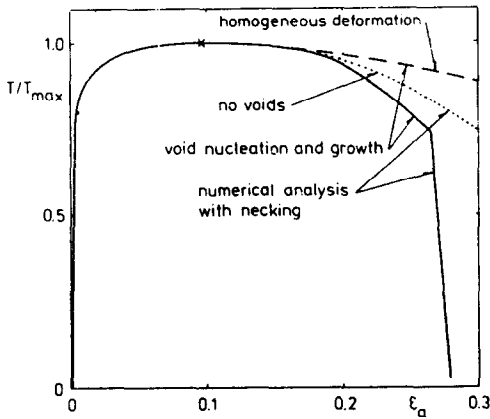


Fig. 9. Load vs average axial strain curves. Numerical results obtained by 20×42 mesh for $L_0/R_0 = 2$.

At the first stage, immediately after the sharp "knee" on the load vs axial strain curve, the critical value of the void volume fraction, $f_c = 0.15$, has just been reached in the centre of the neck. At the second stage the penny-shaped crack has grown to a size comparable with those in Figs 6 and 7; but here the high straining at about 45° from the crack tip is strong enough to turn the crack out of its plane.

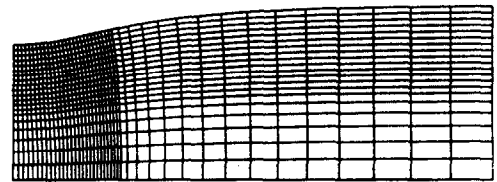
In Figs 11(c) and 12(c) fracture appears to be growing inside a conical shear band, in a way rather similar to the void-sheet fractures found under plane strain tension; but already at this level the growth of a competing failure mechanism is visible in the figures. The next level, Figs 11(d) and 12(d), shows that the inclined crack has actually stopped in its first direction, and has preferred to zig-zag. From the strain contours in Fig. 12(d) it is seen that again a competing zig-zag mechanics has started to grow; but here the first mechanism wins, resulting in the final cup-cone fracture surface indicated in Figs 11(e) and 12(e). It should be noticed that the present computations assume symmetry about the mid-plane, $x^1 = 0$, so that in fact two symmetrical conical fracture surfaces are predicted; but in reality one of these cracks will finally dominate, thus resulting in the cup-cone fracture observed experimentally.

The way crack growth is described here, based on the constitutive law for a porous ductile material, there is a continuous transition from a vanishing stress carrying capacity in the material at the crack tip to a much higher strength at some distance from the tip. The corresponding continuous variation of the void volume fraction approximates a distribution of voids, with those just in front of the crack tip on the verge of coalescence. Effects of a material length scale, such as the void spacing, are not incorporated in the present continuum model of the material response.

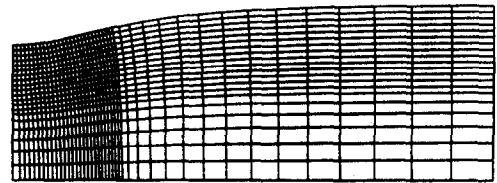
In Fig. 13 the numerical description of the crack is illustrated in more detail by deformed meshes at six different levels, with all fractured (vanished) triangular elements painted black at each level. The first

stage corresponds to $T/T_{\max} = 0.683$ and the last stage is identical with Figs 10(e), 11(e) and 12(e). In the initial part of the crack [Fig. 13(b)] one of the triangular elements is left in each fractured quadrilateral, thus making the cracks as narrow as possible in the chosen mesh. These unfractured triangles are located (by the computation) such that the crack appears to zig-zag from the beginning; but no fracture occurs outside the first column of quadrilaterals before that shown in Fig. 13(c). Also at the final conical parts of the crack the pattern of vanished elements is as narrow as possible.

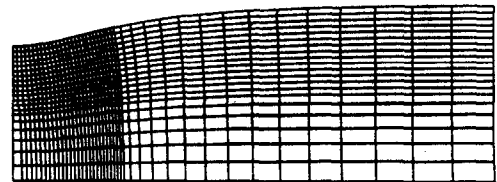
The basic reason for the zig-zag fracture is explained by the development of the solution around the stage shown in Fig. 13(c). Initially, when the crack starts to grow away from the mid-plane ($x^1 = 0$), the



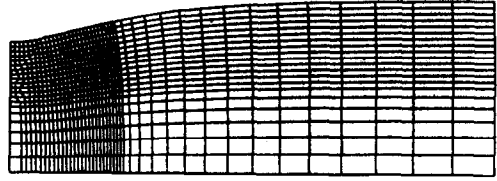
(a)



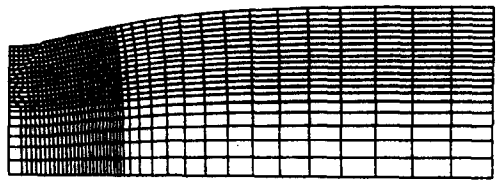
(b)



(c)



(d)



(e)

Fig. 10. Deformed 20×42 meshes for $L_0/R_0 = 2$. (a) $T/T_{\max} = 0.731$, (b) $T/T_{\max} = 0.521$, (c) $T/T_{\max} = 0.431$, (d) $T/T_{\max} = 0.153$, (e) $T/T_{\max} = 0.032$.

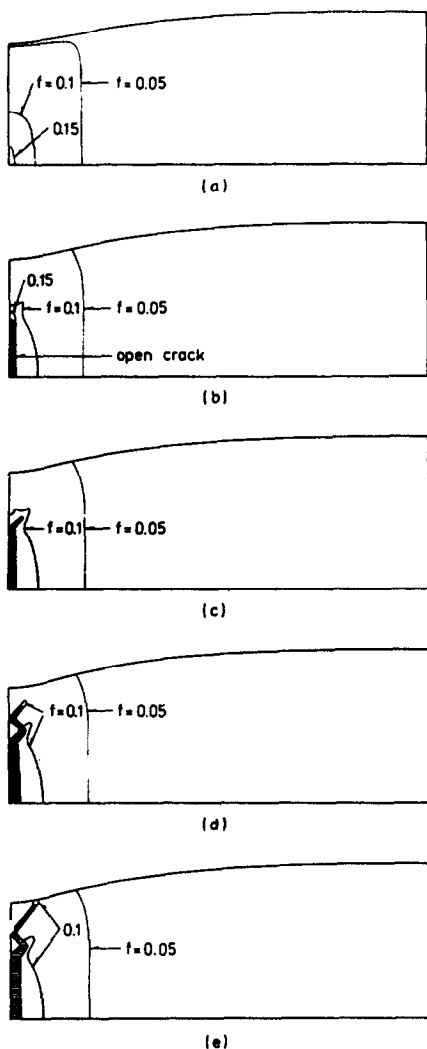


Fig. 11. Curves of constant void volume fraction for $L_0/R_0 = 2$. (a) $T/T_{\max} = 0.731$, (b) $T/T_{\max} = 0.521$, (c) $T/T_{\max} = 0.431$, (d) $T/T_{\max} = 0.153$, (e) $T/T_{\max} = 0.032$.

material between this plane and the crack unloads elastically, as would also be the case for a crack growing into a shear band under strain conditions; but already in Fig. 13(c) this material has again started to yield plastically, due to increasing compressive hoop stresses. In the round bar, continued shear localization on the inclined band initiated in Fig. 13(c) is only possible if the triangular axisymmetric section of the bar between the band and the mid-plane reduces its radius; but this requires a great deal of plastic work, which is avoided by preferring the zig-zag path shown in Fig. 13(d). In the later stage of Fig. 13(e) less material is enclosed between the growing band and the mid-surface, and here crack growth continues along the conical surface. On the other hand, in the earlier stage shown in Fig. 13(b) the restrictive influence of axisymmetry is so strong that the crack does not leave the first column of quadrilaterals, even though the fine meshed region has just been reached.

It is now possible, based on the results discussed above, to speculate on the influence of using a still much finer mesh. Already at a small penny-shaped crack this very fine mesh would predict the intense straining at about 45° from the crack tip, and therefore crack extension away from the mid-plane, on a conical surface, would be expected at a small ratio of crack radius to external neck radius. However, due to the restrictive influence of axisymmetry just discussed, a zig-zag crack is expected, which will remain very near the mid-plane, perhaps with bigger deviations at larger radii. The size of the final conical lip predicted on the fracture surface in Fig. 13(f) is mesh dependent; but with a much finer mesh this lip size relative to the neck radius is expected to approach a quantity characteristic of the material. In this context it is noted that the degree of necking observed on a specimen is clearly a function of the nucleation and failure laws for the particular material, since necking essentially stops when cracking initiates.

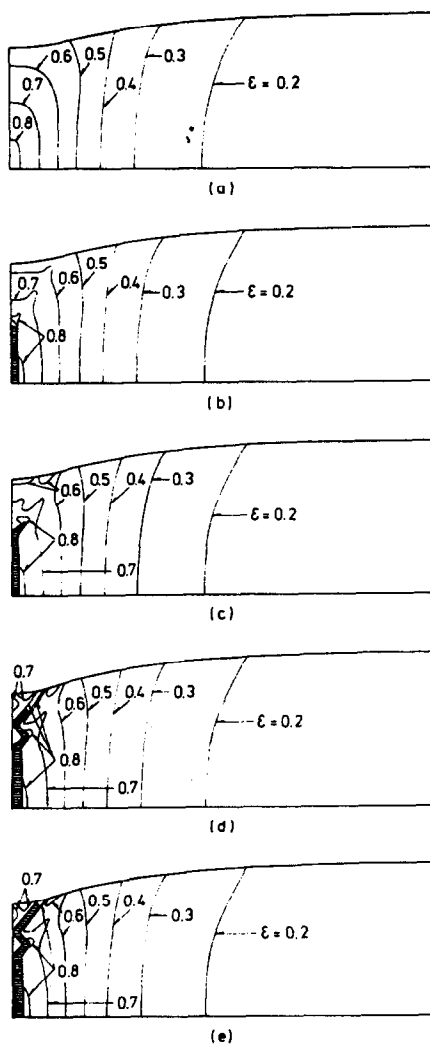


Fig. 12. Curves of constant maximum principal logarithmic strain for $L_0/R_0 = 2$. (a) $T/T_{\max} = 0.731$, (b) $T/T_{\max} = 0.521$, (c) $T/T_{\max} = 0.431$, (d) $T/T_{\max} = 0.153$, (e) $T/T_{\max} = 0.032$.

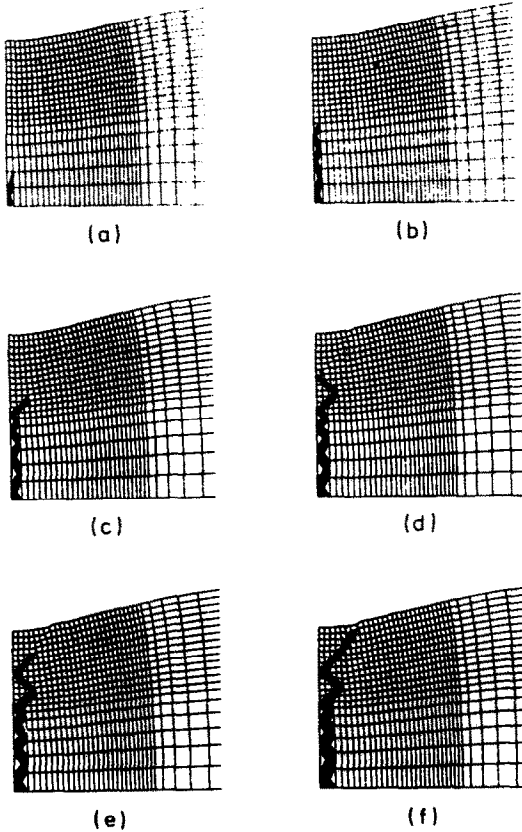


Fig. 13. Crack growth in 20×42 mesh for $L_0/R_0 = 2$. Vanished triangular elements are painted black. (a) $T/T_{\max} = 0.683$, (b) $T/T_{\max} = 0.565$, (c) $T/T_{\max} = 0.438$, (d) $T/T_{\max} = 0.249$, (e) $T/T_{\max} = 0.165$, (f) $T/T_{\max} = 0.032$.

The slope of the last nearly vertical part of the load versus strain curve in Fig. 9 depends on the geometry of the tensile test specimen. For large values of L_0/R_0 the elastic axial contraction under decreasing load will dominate here, and ϵ_a will decay during the crack growth. The same tendency may result from using a much finer mesh in the neck, since the crack opening gives the only positive contribution to the overall extension. In cases where ϵ_a decays on this last part of the quasi-static equilibrium curve, fracture will in practice occur dynamically, if the elongation is prescribed on the test machine.

5. DISCUSSION

The results of the calculations presented here reproduce the essential features of the cup-cone fracture process illustrated in Fig. 1. Voids nucleate and grow in the necked down region with substantial voidage occurring away from the center of the specimen. Fracture initiates at the center of the neck and, initially, the crack propagates across the specimen remaining close to the minimum section. As the crack approaches the free surface, where the axisymmetry has a less constraining effect, the amplitude of the

zig-zag increases, finally forming the cone of the cup-cone fracture.

In each of Figs 6(b), 7(b) and 11 there is a rather large volume fraction of voids, $f = 0.05$, throughout the neck region. The actual volume fraction value depends, of course, on the parameters taken to characterize the material, particularly the nucleation strain, which here is $\epsilon_N = 0.3$. However, the occurrence of extensive voidage throughout the neck region is consistent with a large number of observations, e.g. Puttick [2], Bluhm and Morrissey [1]. What is interesting, though, by way of contrast, is that very high void volume fractions (say greater than 0.1) are confined to a relatively small region near the center of the neck. This arises from the strong sensitivity of void growth (as illustrated in Fig. 3) to the superposed hydrostatic tension, which peaks at the neck center.

In our analysis the loss of load carrying capacity accompanying fracture is incorporated via the function $f^*(f)$ into the flow potential surface (2.2). The values of the parameters characterizing this process have been chosen to be representative, as suggested by observation and analysis, but are not meant to characterize any particular material. The fracture criterion we employ, a critical void volume fraction in conjunction with a porous plastic constitutive relation, is quite different from the use of a phenomenological critical fracture strain. Our criterion does give a critical strain, but one which depends on the stress and deformation history of the material element in which failure ultimately occurs. In accordance with this, fracture in Figs 6, 7 and 11 initiates at a smaller strain than in Fig. 3 since the Bridgman analysis [21], on which Fig. 3 is based, underestimates the peak triaxiality somewhat.

Up to the initiation of fracture the development of necking in the porous plastic solid is qualitatively similar to that in classical plastic solids [18–22]. The onset of fracture is associated with the sharp “knee” in the load deflection curve of Fig. 9, in accord with the observations of Bluhm and Morrissey [1] who did not observe any signs of gross macroscopic fracture prior to the knee of the load deflection curve in their tests. The unloading associated with the initiation of fracture arrests void development except in the region influenced by the crack tip [Fig. 11(b–e)]. Since neck development essentially stops when fracture initiates, our analysis indicates that the reduction in area at failure is a representative measure of the onset of macroscopic fracture in the tensile test. A larger value of the mean strain for nucleation, ϵ_N , would delay the occurrence of a high void volume fraction, and thus increase the area reduction prior to failure.

The kinematic constraint imposed by the axisymmetric geometry plays an important role in the development of the cup-cone fracture. As discussed in the previous section it is this constraint that inhibits the initial tendency of the crack to leave the plane of the neck. On the basis of the present calculation it

cannot be stated whether the zig-zag of the crack in the initial stages of deformation exhibited in Fig. 13 is real or is a mesh effect. In any case, in the early stages of development the crack is confined to the first row of elements.

In the above discussion the completely failed material region has been referred to as a crack. This is a convenient terminology for referring to a region that has undergone a complete loss of stress carrying capacity, but does not refer to a crack in the usual sense. In our formulation, the distinction between the crack and the surrounding material is not completely sharp, since the void volume fraction varies continuously. Thus, the stress carrying capacity of the material in front of the crack tip grows continuously from the value zero at the tip.

In any case, once the crack (or failed material region) has progressed about half way through the specimen, the axisymmetry constraint is reduced sufficiently for shearing out of the plane of the crack to be accommodated with a sufficiently small inward displacement of the triangular region between the shear band and the plane of the neck. In Fig. 12 (c and following) a band of high strain is visible all the way to the surface. At least part of the reason for the relatively long range effect of the strain concentration in front the crack is associated with the near loss of ellipticity in the highly porous neck region with the strains propagating along the emerging characteristic directions. In fact the direction of propagation is in reasonable agreement with what would be expected based on a shear band analysis [15]. The subsequent change in direction of the crack arises from the kinematic constraint imposed by the axisymmetry, as mentioned previously.

By way of contrast, in plane strain tension there is no such geometrical constraint on shearing. The inward displacement of the corresponding triangular region is only associated with a rigid translation so that a shear band, once initiated, can propagate through the specimen. The change in fracture mode with deformation state is clearly illustrated by Speich and Spitzig [38, Fig. 23], where the same material is shown to exhibit a cup-cone failure in axisymmetric tension and a macroscopic shear failure in plane strain tension.

In fact, plane strain calculations carried out by Tvergaard [28] using a porous plastic material model incorporating a final failure criterion much like the one used here does exhibit the propagation of a crack across the thickness. The crack initiates in a shear band and propagates along this band. In the plane strain calculation the angle of inclination of the shear bands is in good agreement with that predicted by a localization analysis (Tvergaard [28]). In the axisymmetric tension case considered here the relation between the critical angle given by a shear band analysis and the angle of crack propagation is not so straightforward.

As discussed in the previous section there are

important mesh effects encountered in the analysis. It should also be noted that, as in previous analyses of highly localized deformation modes, the question of mesh dependent length scales arises. The constitutive relation we have employed contains no material dependent length scale. As already alluded to, the initial zig-zag of the crack near the neck center depicted in Fig. 13 may be an artifact of the mesh. In any case incorporation of a material dependent length scale into a constitutive framework of the sort employed here would be useful, not only for further studies of the failure process in a round tensile bar, but also in applications of this type of analysis in the region near a sharp crack.

Acknowledgement—A.N. gratefully acknowledges the support of the U.S. National Science Foundation (Solid Mechanics Program) through grant MEA-8101948.

REFERENCES

1. J. I. Bluhm and R. J. Morrissey, *Proc. 1st Int. Conf. Fract.*, Vol. 3, 1739 (1966).
2. K. E. Puttick, *Phil. Mag.* **5**, 759 (1960).
3. S. H. Goods and L. M. Brown, *Acta metall.* **27**, 1 (1979).
4. F. A. McClintock, *J. appl. Mech.* **35**, 363 (1968).
5. J. R. Rice and D. M. Tracey, *J. Mech. Phys. Solids* **17**, 201 (1969).
6. T. B. Cox and J. R. Low, *Metall. Trans.* **5**, 1457 (1974).
7. H. C. Rogers, *Trans. T.M.S.-A.I.M.E.* **218**, 498 (1960).
8. G. Green and J. F. Knott, *J. Engng Mater. Tech.* **98**, 37 (1976).
9. J. W. Hancock and A. C. Mackenzie, *J. Mech. Phys. Solids* **24**, 147 (1976).
10. L. M. Brown and J. D. Embury, *Proc. 3rd Int. Conf. on Strength of Metals and Alloys*, p. 164 (1973).
11. A. L. Gurson, *J. Engng Mater. Tech.* **99**, 2 (1977).
12. A. L. Gurson, *Porous Rigid-Plastic Materials Containing Rigid Inclusions—Yield Function, Plastic Potential, and Void Nucleation*, *Proc. Int. Conf. Fracture* (edited by D. M. R. Taplin), Vol. 2A, 357. Pergamon Press, Oxford (1977).
13. C.-C. Chu and A. Needleman, *J. Engng Mater. Tech.* **102**, 249 (1980).
14. V. Tvergaard, *Int. J. Fract.* **17**, 389 (1981).
15. M. Saje, J. Pan and A. Needleman, *Int. J. Fract.* **19**, 163 (1982).
16. V. Tvergaard, *Int. J. Solids Struct.* **18**, 659 (1982).
17. V. Tvergaard, *J. Mech. Phys. Solids* **30**, 265 (1982).
18. A. Needleman, *J. Mech. Phys. Solids* **20**, 111 (1972).
19. D. M. Norris, B. Moran, J. K. Scudder and D. F. Quinones, *J. Mech. Phys. Solids* **26**, 1 (1978).
20. M. Saje, *Int. J. Solids Struct.* **15**, 731 (1979).
21. P. W. Bridgman, *Studies in Large Plastic Flow and Fracture*. McGraw-Hill, New York (1952).
22. A. S. Argon, J. Im and A. Needleman, *Metall. Trans.* **6A**, 815 (1975).
23. A. S. Argon, J. Im and R. Safoglu, *Metall. Trans.* **6A**, 825 (1975).
24. A. S. Argon and J. Im, *Metall. Trans.* **6A**, 839 (1975).
25. J. W. Hancock and D. K. Brown, *J. Mech. Phys. Solids* **31**, 1 (1983).
26. V. Tvergaard, *Int. J. Fracture* **18**, 237 (1982).
27. H. Andersson, *J. Mech. Phys. Solids* **25**, 217 (1977).
28. V. Tvergaard, *J. Mech. Phys. Solids* **30**, 399 (1982).
29. A. Needleman and J. R. Rice, *Mechanics of Sheet Metal Forming* (edited by D. P. Koistinen et al.), p. 237. Plenum Press, Oxford (1978).
30. J. Gurland, *Acta metall.* **20**, 735 (1972).

31. C. A. Berg, *Inelastic Behaviour of Solids* (edited by M. F. Kanninen *et al.*), p. 171. McGraw-Hill, New York (1970).
32. A. Needleman and V. Tvergaard, *On the Finite Element Analysis of Localized Plastic Deformation*. Division of Engineering, Brown University (1982).
33. J. W. Hutchinson and J. P. Miles, *J. Mech. Phys. Solids* **22**, 61 (1974).
34. B. Raniecki and O. T. Bruhns, *J. Mech. Phys. Solids* **29**, 153 (1981).
35. H. Yamamoto, *Int. J. Fracture* **14**, 347 (1978).
36. V. Tvergaard, A. Needleman and K. K. Lo, *J. Mech. Phys. Solids* **29**, 115 (1981).
37. M. Y. He and J. W. Hutchinson, *The Penny-Shaped Crack in a Round Bar of Power-Law Hardening Material*. Division of Appl. Sci., Harvard University (1981).
38. G. R. Speich and W. A. Spitzig, *Metall. Trans.* **13A**, 2239 (1982).